SCIENCE CHINA
Information Sciences

• RESEARCH PAPER •

September 2026, Vol. 69, Iss. 9, 192403:1–192403:14
https://doi.org/10.1007/s11432-025-4871-2

Ultralow-crosstalk, microsecond-response resonant SAW multidimensional force sensor for robotic arm integration

Fen LI, Xiaojuan HOU*, Xin ZHANG, Huipeng ZHAO, Weichun GAO, Sha HU, Zhe WANG, Wenping GENG, Jian HE* & Xiujian CHOU

Science and Technology on Electronic Test and Measurement Laboratory, North University of China, Taiyuan 030051, China

Received 31 October 2025/Revised 31 December 2025/Accepted 17 March 2026/Published online 12 August 2026

Abstract The autonomous operation of robots and spacecraft manipulators imposes stringent requirements on multidimensional force sensors for tasks such as grasping, assembly, and collaboration, under complex dynamics and nonuniform contacts that demand high accuracy. This study introduces a resonant surface acoustic wave (SAW) multidimensional force sensor on a 128° YX $LiNbO_3$ substrate, and the sensor utilizes force-acoustic-electric conversion to achieve microsecond-level response and axis decoupling. The 128° YX $LiNbO_3$ substrate offers strong piezoelectric coupling, high acoustic velocity, and pronounced anisotropy, which enhances electromechanical coupling and boosts frequency sensitivity along the X axis, improving directional selectivity and reducing cross-axis crosstalk. The sensor features a cross-beam/vertical-beam composite frame that supports multiple symmetrically mounted SAW resonators, each primarily responsive to its designated sensitive direction. Differential readouts provide decoupled X- and Y-axis outputs, and the averaged output is used for Z. The interdigital transducer (IDT) pairs, wavelength, reflector pairs, and IDT-reflector separation are optimized through parametric design sweeps to balance sensitivity against bandwidth. Finite-element modeling refines global parameters to enhance stiffness and suppress coupling. Experimental results demonstrate a linear frequency-force relationship, with sensitivities of 1794.64, 1607.14, and 403.41 $Hz \cdot N^{-1}$ for the X, Y, and Z axes, respectively, while crosstalk remains below 1%. Integrated into a robotic arm end-effector, the sensor tracks three-axis contact forces during controlled contact and collision events, supporting reliable force control and safe human-machine interaction in advanced manufacturing.

Keywords surface acoustic wave (SAW), multidimensional force sensors, 128° YX $LiNbO_3$, ultralow-crosstalk, robotic arm

Citation Li F, Hou X J, Zhang X, et al. Ultralow-crosstalk, microsecond-response resonant SAW multidimensional force sensor for robotic arm integration. Sci China Inf Sci, 2026, 69(9): 192403, https://doi.org/10.1007/s11432-025-4871-2

1 Introduction

With the rapid advancement of intelligent manufacturing and robotic technology, the demand for precise multidimensional force control and feedback in robotic manipulators [1, 2] and other complex mechanical systems has steadily increased. Although conventional force sensing technologies—such as resistive strain gauges [3–6], piezoelectric sensors [7, 8], capacitive sensors [9–11], and fiber optic sensors [12, 13]—are mature, they often suffer from limited sensitivity and bandwidth, as well as increased fabrication and packaging costs in multidimensional measurements. As a result, achieving high accuracy and high sensitivity while ensuring robust inter-axis decoupling remains a significant challenge. In recent years, substantial progress has been made in multidimensional force sensing. Zhao et al. [14] reported a resonant force sensor that integrates an optimized layout of piezoelectric elements with an elastic structure, achieving intrinsic frequency errors of 3.0%, 0.19%, and 0.19% along the three axes. Li et al. [15] fabricated a flexible PVDF film piezoelectric tactile sensor capable of three-dimensional force measurement, demonstrating high sensitivity, fast response, and good repeatability under continuous loading. Li et al. [16] explored a fault-tolerant mechanism for a piezoelectric six-dimensional force sensor and performed static calibration of a four-point-supported prototype under unidirectional loads, under both normal operation and signal-loss scenarios. Despite these advances in piezoelectric layout design, material selection, and optimization algorithms, simultaneously satisfying stricter requirements—such as miniaturization, broad bandwidth, and electromagnetic immunity—remains challenging.

Surface acoustic wave (SAW) devices [17–19] have attracted considerable attention because of their passive operation, immunity to electromagnetic interference, ease of miniaturization, and intrinsically linear frequency output. $LiNbO_3$ [20], which combines strong piezoelectricity with a high acoustic velocity, is widely employed in the

* Corresponding author (email: houxiaojuan@nuc.edu.cn, drhejian@nuc.edu.cn)

design and fabrication of SAW sensors [21,22]. In particular, 128° YX $LiNbO_3$ [23,24] offers a large electromechanical coupling coefficient and favorable temperature characteristics, which help maintain a stable and approximately linear resonant-frequency response under mechanical loading. Duan et al. [25] fabricated a multilayer SiO_2/AlN/SOI structure via a MEMS-compatible process for SAW micro-pressure sensors and introduced a cantilever beam inertial structure to enhance sensitivity. Kohler et al. [26] employed an SAW device on 128° YX $LiNbO_3$ as a force myography sensor, enabling real-time monitoring of muscle contractions with high sensitivity and accuracy. Li et al. [27] reported an integrated SAW sensor for simultaneously temperature and strain sensing, achieving a strain sensing range of 0–700 με and a sensitivity of 100 $\text{Hz}\cdot\mu\varepsilon^{-1}$. However, existing multidimensional SAW sensors are generally restricted to low loads ($< 100\,\text{N}$), limited to two axes, or affected by structural coupling, directional crosstalk, and uneven sensitivity, which restrict their use in high-load, high-precision, and low-crosstalk applications.

To address these limitations, a piezoelectric multidimensional force sensor integrating resonant SAW devices on 128° YX $LiNbO_3$ is proposed. The sensor features a cross-beam/vertical-beam architecture. Electromechanical coupling characteristics are modeled in COMSOL Multiphysics, and the structural dimensions, resonator placement, and loading conditions are systematically optimized to achieve high linearity and sensitivity. Differential readout increases the X- and Y-axis sensitivities compared with single-resonator readout, while cross-axis crosstalk remains below 1%. The design uses only six SAW resonators, obviating the need for a Wheatstone bridge; surface stress is encoded directly as a resonant frequency shift (Δf). Across load ranges of 0–500 N for X/Y and 0–1000 N for Z, the sensor shows linear fits with $R^2 \geqslant 0.99$ while maintaining ultralow directional crosstalk. The resulting 128° YX $LiNbO_3$ resonant SAW multidimensional force sensor (SAWMFS) is well suited for high-load, multidimensional measurement scenarios, meeting the requirements of high-bandwidth applications such as high-speed robotic force control, precision assembly, and collision detection.

2 Results and discussion

2.1 Design and characterization of the SAWMFS

A multidimensional force sensor simultaneously measures forces along the X, Y, and Z axes. In robotic manipulators and related systems, such a device enables real-time monitoring of end effector interactions with the surrounding environment, thereby facilitating compliant grasping, trajectory optimization, and safe collision avoidance (Figure 1(a)). A SAW-based multidimensional sensor transduces load-induced structural stress/strain into small shifts in resonant frequency through the piezoelectric effect [28]. The sensing element consists of interdigitated transducers (IDTs) patterned on a 128° YX $LiNbO_3$ substrate. An electric field applied to the input IDT launches Rayleigh waves, which are converted back into an electrical response at the output IDT. For multidimensional sensing with reduced directional crosstalk, multiple SAW resonator pairs are bonded to the horizontal beams (Figure 1(b)). Within each pair, the two resonators respond with equal-magnitude Δf of opposite sign under beam loading. For example, a $+X$-directed force applied at the central annular region shifts the central ring rightward, placing the left horizontal beam in tension and the right beam in compression. The SAW devices on these beams experience axial strains of equal magnitude but opposite sign: tensile strain on the left increases the electrode pitch and lowers the resonant frequency, whereas compressive strain on the right decreases the pitch and raises the frequency. With an approximately strain-proportional frequency response, the two resonators show mirrored behavior: the left resonator shifts to a lower frequency, whereas the right shifts to a higher frequency. Taking the frequency difference approximately doubles the sensitivity and suppresses common-mode disturbances (e.g., temperature drift), yielding a high accuracy, temperature-robust force signal. The Y-axis pair follows the same differential principle. For Z-axis loading, the two SAW devices attached to the vertical beam experience nearly identical Δf; the axial force is therefore determined by averaging the two frequencies. Under single-axis loading, the corresponding SAW resonator pair produces the dominant frequency response (Figure 1(c)). After differential/averaged processing, contributions from the non-sensing axes remain very small, resulting in low crosstalk. External forces are transmitted through the beam structure to the resonator surface. When the load reaches the SAW devices, two mechanisms contribute to the Δf (Figure 1(d)). First, mechanical loading stretches or compresses the piezoelectric substrate, altering the IDT geometry and thereby the acoustic wavelength. Second, stress can perturb material properties (e.g., elastic constants and density), which changes the surface wave velocity. The combined effects shift the resonant frequency of the SAW device.

When a single-port resonant SAW sensor is designed (Figure 1(e)), its structural parameters require careful optimization to maximize performance [29]. For a uniform interdigital transducer (IDT), key geometric variables include the finger width, the number of IDT pairs N_i, the acoustic aperture L_i, the number of reflector pairs N_r,

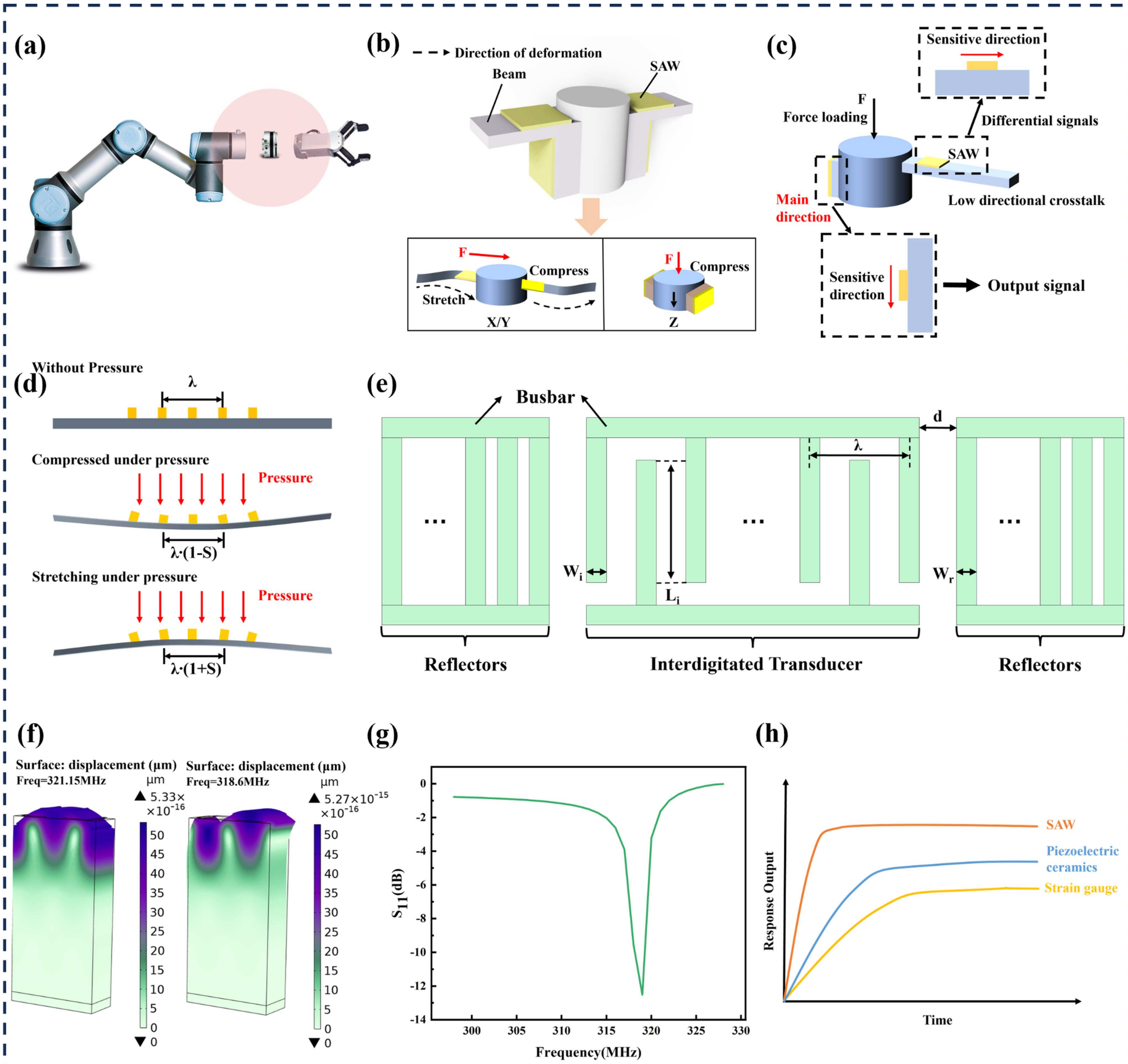

Figure 1 (Color online) Working principle and simulation analysis of SAWMFS. (a) SAWMFS applied in a robotic manipulator; (b) tensile and compressive strains in different directions; (c) patching method; (d) changes of SAW under tension and compression; (e) SAW device; (f) resonant frequency under symmetric mode and antisymmetric mode; (g) simulated S_{11} response of the resonator; (h) response time.

and the separation d between the IDT and the reflector.

Increasing N_i strengthens electromechanical coupling and therefore improves acoustic to electrical conversion efficiency. However, it also increases the radiation conductance G and the associated power dissipation [30]. The parameter G is given by (1), where C is the capacitance per unit IDT length, f_0 is the resonant frequency, k^2 is the electromechanical coupling coefficient, and W is the acoustic aperture.

$$G = 8Cf_0k^2WN_t. \tag{1}$$

For a uniform IDT, the amplitude-frequency response is described by (2), and the −3 and −4 dB relative bandwidths are defined in (3) and (4).

$$|H_m(f)| = \pi N_t \frac{f - f_m}{f_0}, \tag{2}$$

$$BW_{-3\text{ dB}} = \frac{0.885}{N_t}, \tag{3}$$

$$BW_{-4\text{ dB}} = \frac{1}{N_t}. \tag{4}$$

Table 1 SAW resonator structural design parameters.

Parameter	Symbol	Value	Parameter	Symbol	Value
Bar-width of IDT	W_i	3 μm	Metallization of IDT/reflector	η	0.5
Bar-width of reflector	W_r	3 μm	Wavelength	λ	12 μm
Pairs of IDTs	N_i	100	Separation between IDT and reflector	d	21 μm
Pairs of reflectors	N_r	150	Cr electrode	t_1	20 nm
Acoustic aperture	L_i	1200 μm	Au electrode	t_2	100 nm

Eqs. (2)–(4) show that the response magnitude increases linearly with N_i, and the corresponding bandwidth narrows as N_i increases [31]. This trend imposes a design trade-off: an overly large N_i increases device size and fabrication complexity, whereas too small a value fails to sufficiently suppress spurious modes. Accordingly, N_i is set to 100 in this design.

The acoustic aperture ω affects the resonator amplitude, diffraction loss, transverse modes, and insertion loss [32]. A larger ω strengthens electromechanical coupling, increases effective capacitance and signal amplitude, and reduces insertion loss, but may degrade high-frequency stability; conversely, a smaller ω intensifies SAW diffraction. Therefore, ω should be selected to balance these competing effects. In practical designs, values between 10 and 100 λ are typically adopted, where λ is the acoustic wavelength. In this design, ω is set to 100 λ.

The reflectivity of the grating mirrors is a key design parameter and is primarily determined by the number of reflector pairs N_r, as given by (5). Increasing N_r raises the reflection coefficient and consequently the quality factor Q, which improves frequency resolution [33, 34].

$$\Gamma = \tanh\left(N_r\left|\frac{\Delta Z}{Z}\right|\right). \tag{5}$$

Here, $\Delta Z/Z$ represents the acoustic-impedance mismatch at the electrode edges. Because Q does not increase indefinitely in practice, N_r should be chosen judiciously. Following the empirical rule in (6), N_r is set to 150 in the present design.

$$N_r\left|\frac{\Delta Z}{Z}\right| \approx 3\text{–}4. \tag{6}$$

The separation d between the IDT and reflector extends the propagation path of the reflected wave, which can attenuate spurious modes and suppress sidelobes. Excessive spacing increases propagation loss and reduces wave amplitude [35]. The gap must also satisfy the Bragg condition associated with the chosen reflector type.

$$L_g = \begin{cases} (n-0.5)\dfrac{\lambda}{2}, & (Z_m < 1), \\ n\dfrac{\lambda}{2}, & (Z_m > 1). \end{cases} \tag{7}$$

In this formulation, Z_m is the acoustic impedance parameter ($Z_m > 1$ for open-circuit gratings and $Z_m < 1$ for short-circuit gratings) and n is a positive integer. Using short-circuit reflectors with $n = 4$ yields $d = 21$ μm. The final structural parameters of the SAW resonator are summarized in Table 1.

In a SAWMFS, the achievable frequency sensitivity scales with the center frequency (f_0), the electromechanical coupling coefficient (k^2), and the quality factor (Q), and is ultimately limited by the frequency-noise floor. Accordingly, increasing f_0, k^2, and Q while reducing the noise floor improves the frequency sensitivity of the SAW sensor. A finite-element model of the sensor is built in COMSOL Multiphysics by coupling the solid mechanics and electrostatics modules, using the parameters listed in Table 1. Because the IDT contains several hundred identical finger pairs with lengths far exceeding their widths, edge effects are expected to be small and can be neglected. The model is therefore reduced to a periodic unit cell. As illustrated in Figure S1, this simplification preserves accuracy while substantially reducing computational cost, thereby accelerating the design process [36]. Resonant frequency analysis of a SAW resonator typically focuses on the symmetric and antisymmetric modes. Within the frequency window of interest, COMSOL returns both modes (Figure 1(f)). The effective SAW velocity $V_{\rm eff}$ is extracted from the symmetric (f_{sc^-}) and antisymmetric (f_{sc^+}) resonant frequencies [37]. Substituting the simulated values into (8) yields a velocity that agrees well with the theoretical acoustic velocity of $LiNbO_3$. The corresponding S_{11} response curve (Figure 1(g)) shows a resonant frequency of 319.14 MHz for the selected mode. Figure 1(h) compares the response time of SAW, piezoelectric ceramics (PZT), and resistance strain gauges, indicating a markedly faster response for the SAW device.

$$V_{\rm eff} = \lambda\left(\frac{f_{sc^-} + f_{sc^+}}{2}\right). \tag{8}$$

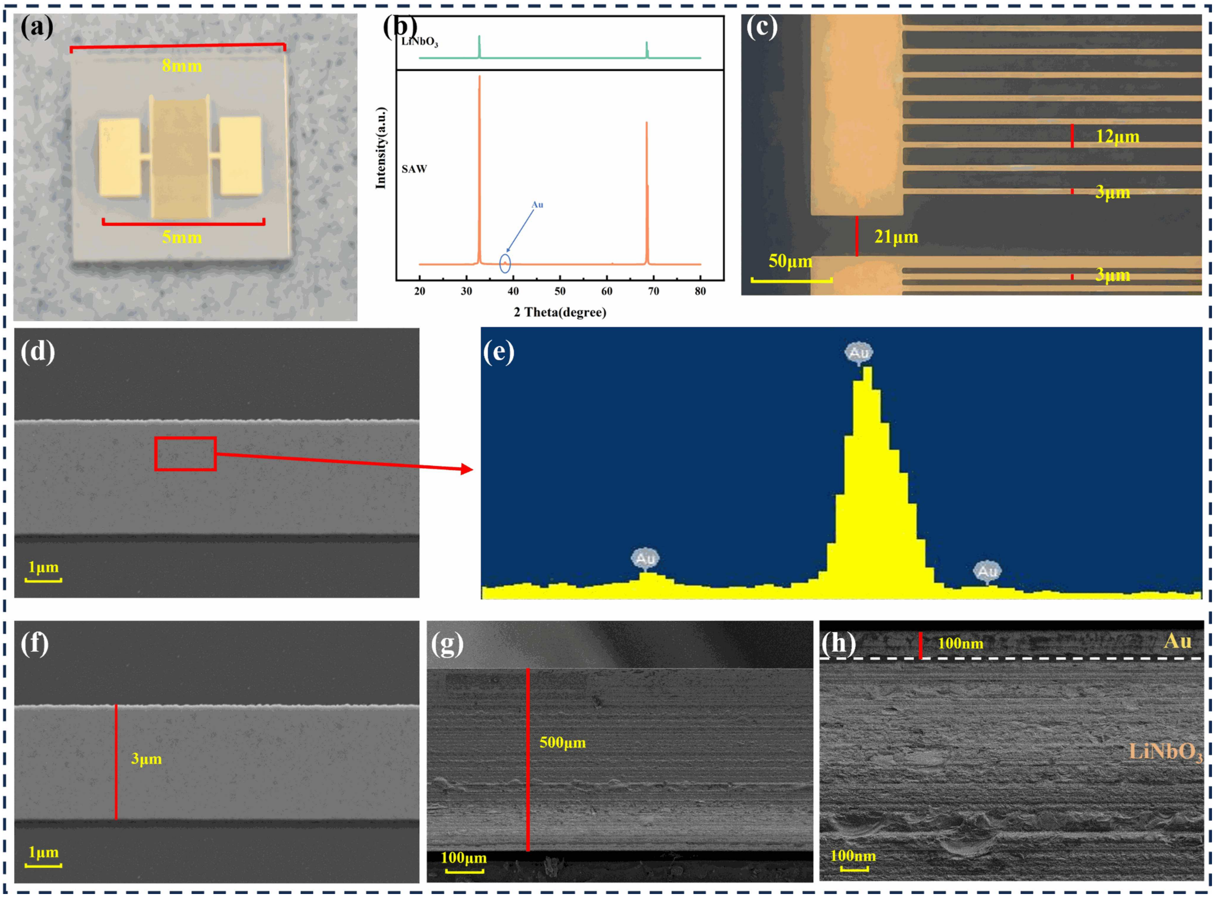

Figure 2 (Color online) Structural characterization of the SAW device. (a) SAW device; (b) XRD patterns of SAW and pure $LiNbO_3$; (c) wavelength and spacing between IDT and reflector; (d) IDT; (e) EDS map of the framed area in (d); (f) IDT line width; (g) cross-sectional view of the SAW structure; (h) Au and $LiNbO_3$ heterointerface.

The scanning electron microscope (SEM, Sigma-300, Zeiss, Germany) and energy dispersive X-ray spectroscopy (EDS) were used to characterize the layered structure of the SAW device. Figure 2 presents the SEM, EDS, and X-ray diffraction (XRD) results. A photograph of the finished sensor is shown in Figure 2(a); the overall chip measures 8 mm × 8 mm with an active area of 5 mm × 5 mm. The XRD pattern in Figure 2(b) displays the characteristic diffraction peaks of $LiNbO_3$, confirming that the substrate is a high-crystallinity single crystal. Additional reflections at 32.8° and 68.5° are consistent with a 128° YX $LiNbO_3$ wafer and further support its good crystallinity. Key structural parameters are indicated in Figures 2(c) and (f), including an IDT finger width of 3 μm, an acoustic wavelength of 12 μm, and a 21 μm gap between the IDT and the reflector array. Figure 2(e) presents the EDS spectrum obtained from the boxed region in Figure 2(d), where prominent Au peaks identify the electrode material. Structural characterization of the device on a $LiNbO_3$ substrate is shown in Figures 2(g) and (h). The cross-sectional SEM images show the metal electrodes deposited on the wafer. The magnified view shows a sharp interface between the gold (Au) layer and the substrate, suggesting uniform deposition and good adhesion. These geometric choices support efficient acoustic excitation and reflection within the target frequency band and provide a reliable structural basis for stable resonant operation in sensing applications.

2.2 Structural design

The sensor comprises an annular outer frame, an internal cross-beam assembly, and a vertical-beam (Figure 3(a)). Stainless steel is selected for the housing to provide rigid mounting and reduce susceptibility to environmental disturbances. The cross-beam assembly comprises four radially oriented arms, each carrying a SAW resonator at its free end. Beams 1 and 3 are symmetrically arranged along the X-axis and assigned to X-direction force sensing. Because these beams experience opposite strains, their SAW outputs are processed in differential mode to enhance sensitivity and suppress common mode interference. Beams 2 and 4 are symmetrically arranged along the Y-axis and are used for Y-direction measurements. An additional SAW device is bonded to the vertical-beam to monitor Z-

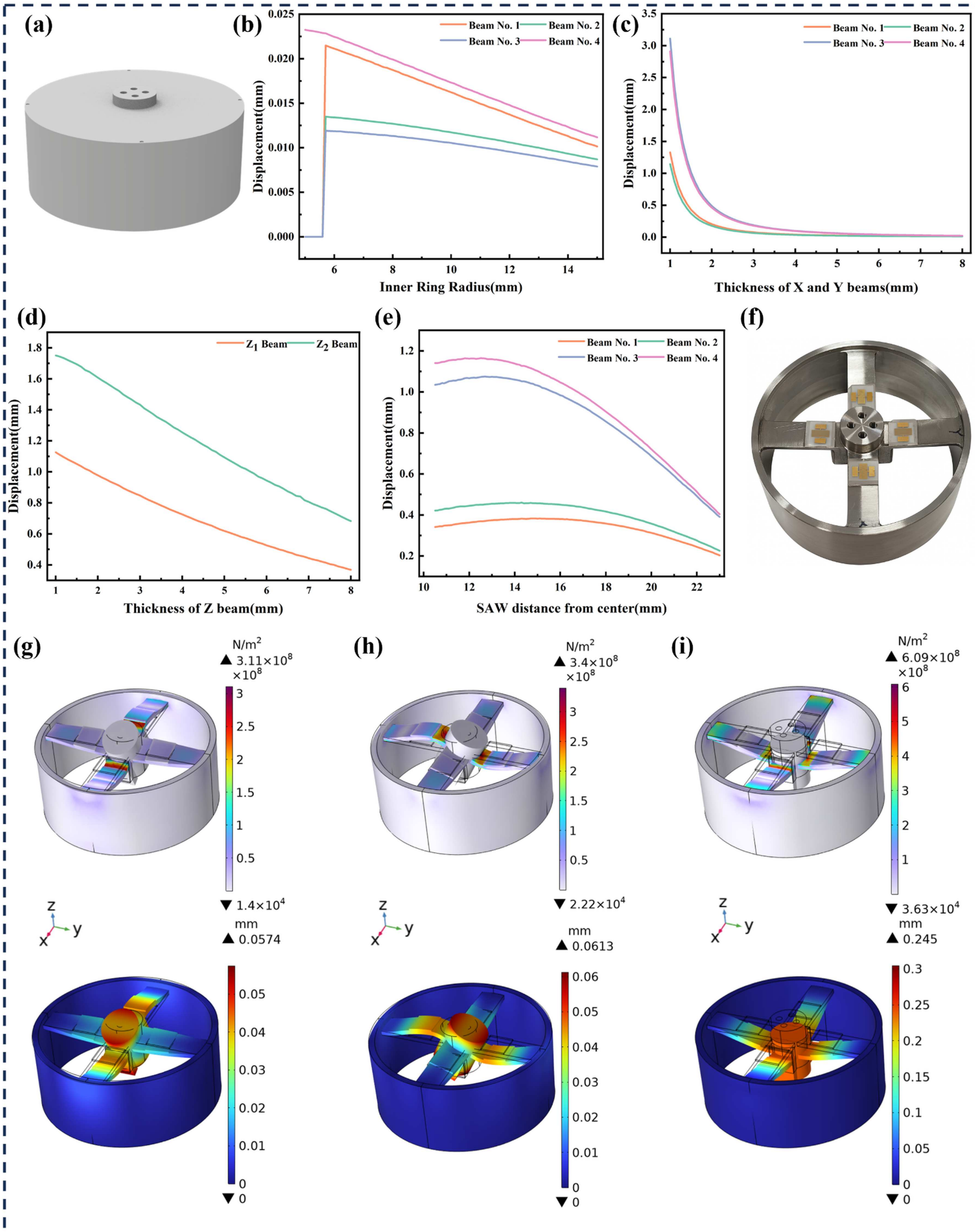

Figure 3 (Color online) Structural simulation analysis of the SAWMFS. (a) Sensor model; (b) inner ring radius; (c) thickness of (X) and (Y) beams; (d) thickness of (Z) beam; (e) SAW distance from center; (f) internal structure; (g) simulated stress and displacement under X-direction loading; (h) simulated stress and displacement under Y-direction loading; (i) simulated stress and displacement under Z-direction loading.

direction forces. To exploit the strong X-axis sensitivity of 128° YX $LiNbO_3$ resonators, each device is rotated so that its sensitive axis aligns with the corresponding load direction. To improve frequency sensitivity and reduce crosstalk while meeting the design loads (F_x, $F_y \geqslant 500$ N; $F_z \geqslant 1000$ N), four geometric parameters are swept parametrically in COMSOL (Figures 3(b)–(e)). The sensor mounting surface is fully constrained, whereas the remaining outer surfaces are treated as traction-free boundaries. The triaxial loads are applied to an equivalent loading surface in the central region of the structure, with directions along the positive X, Y, and Z axes, respectively. A free tetrahedral mesh is adopted, with local refinement at the beam roots and resonator-mounting regions to capture steep stress gradients accurately. The elastic body is modeled as homogeneous material with a Young's modulus $E = 200$ GPa, Poisson's ratio $\nu = 0.3$, and density $\rho = 8000$ kg·m^{-3}.

When the inner-ring radius R is increased from 5 to 15 mm, the beam deflection peaks at $R \approx 5.7$, and then decreases in an approximately linear manner (Figure 3(b)); an overly large R therefore tends to increase the overall stiffness. Balancing sensitivity against structural strength, R is set to 6 mm. As the cross-beam thickness t_{XY} increases, the deformation amplitude and sensitivity drop sharply, whereas an excessively thin beam risks plastic deformation. Figure 3(c) indicates that $t_{XY} = 1.5$ mm provides a practical compromise. The vertical-beam thickness t_Z strongly affects the global stiffness, and Figure 3(d) shows that additional stiffening is marginal for $t_Z \geqslant 4$ mm. Accordingly, t_Z is set to 4 mm to provide a safety margin under a load of 1000 N. Sensitivity increases as the SAW device is placed closer to the center. Figure 3(e) identifies 11–15 mm as the preferred range, and 14 mm is selected to balance sensitivity and manufacturability. The optimized model is shown in Figure 3(f) with $R = 6$ mm, $t_{XY} = 1.5$ mm, $t_Z = 4$ mm, and a 14 mm SAW-to-center distance, providing a robust basis for 0–1000 N simulations and experimental validation.

A finite element model is constructed in COMSOL to evaluate the mechanical performance and resonant response. The solid-mechanics and piezoelectric SAW modules are coupled to compute stress distributions, displacement fields, and load dependent S_{11} parameters. Figures 3(g)–(i) show that X- and Y-direction loads produce modest tip deflections, with stress mainly localized at the beam roots, which is consistent with high structural stiffness and measurement linearity. By contrast, Z-direction loading induces larger beam deflection and higher peak stress, highlighting elevated vertical sensitivity, which is advantageous for axial-load isolation. The maximum von Mises stress is 60.4 MPa, well below the typical yield strength of stainless steel, confirming adequate mechanical strength and safety. The stress distribution is largely uniform, with only minor local concentrations that are not expected to compromise stability or long-term durability.

To assess the directional selectivity of the structure-device arrangement and to support the decoupling model, uniaxial static finite-element analyses are performed in COMSOL on the composite beam structure. Displacements at each SAW mounting region are extracted under three uniaxial loading cases, F_x, F_y, and F_z (Figures S2(a)–(c)). The results show that, under loading along a given axis, the displacement at the corresponding SAW location is markedly larger than the responses at the other locations. The responses in the non-corresponding directions are reduced to near zero after differential processing. For cross-axis comparison, Figure S2(d) summarizes the displacement magnitudes across X, Y, and Z under the three uniaxial loading cases on a logarithmic scale. The dominant response appears in the corresponding loading direction, while the non-corresponding directions remain one or more orders of magnitude smaller. These simulation results indicate clear directional selectivity and limited inter-axis coupling under uniaxial loading.

Although the intrinsic response of a SAW resonator can be on the order of microseconds, the effective bandwidth of the complete force sensor is limited by the natural frequencies of the elastic structure. To eliminate the influence of structural resonance on the experimental results, a modal analysis was performed on the cross-beam/vertical beam composite structure. The first natural frequency is calculated as $f_1 = 2111.8$ Hz (mode shape in Figure S3), and higher-order modes occur at higher frequencies. Because the experimental loading frequency fload is much lower than f_1, structural resonance is unlikely to affect the measured Δf under the present test conditions.

2.3 Performance of the SAWMFS

The measurement platform comprises a microcomputer-controlled electronic universal testing machine, the SAW sensor, and a vector network analyzer (VNA) (Figure 4(a)). This setup records the resonant frequency responses when external forces are applied along the X, Y, and Z. Combining a high-precision loading apparatus with high-resolution frequency readout enables accurate, stable, and real-time data acquisition for multidimensional force calibration and characterization.

In the following, the resonant Δf is used as the output metric. The resonant frequency of the SAW device under zero load (or a defined reference load) is denoted by f_0, and the resonant frequency under load is denoted by f. The Δf is defined as (9). Based on the symmetrical arrangement, the three-axis outputs are obtained using differential readout for the X/Y axis and averaging for the Z, as shown in (10).

$$\Delta f = f - f_0, \tag{9}$$

$$\begin{cases} \Delta f_X = \Delta f_{X1} - \Delta f_{X2}, \\ \Delta f_Y = \Delta f_{Y1} - \Delta f_{Y2}, \\ \Delta f_Z = \dfrac{\Delta f_{Z1} + \Delta f_{Z2}}{2}. \end{cases} \tag{10}$$

The experiments use independent single-axis loading: one axial load is applied at a time, while the other two axes are kept unloaded. The sensitivity along each axis is obtained by linear fitting of the corresponding single-axis calibration curve over the selected linear range. For X-axis loading as an example, the three-axis outputs

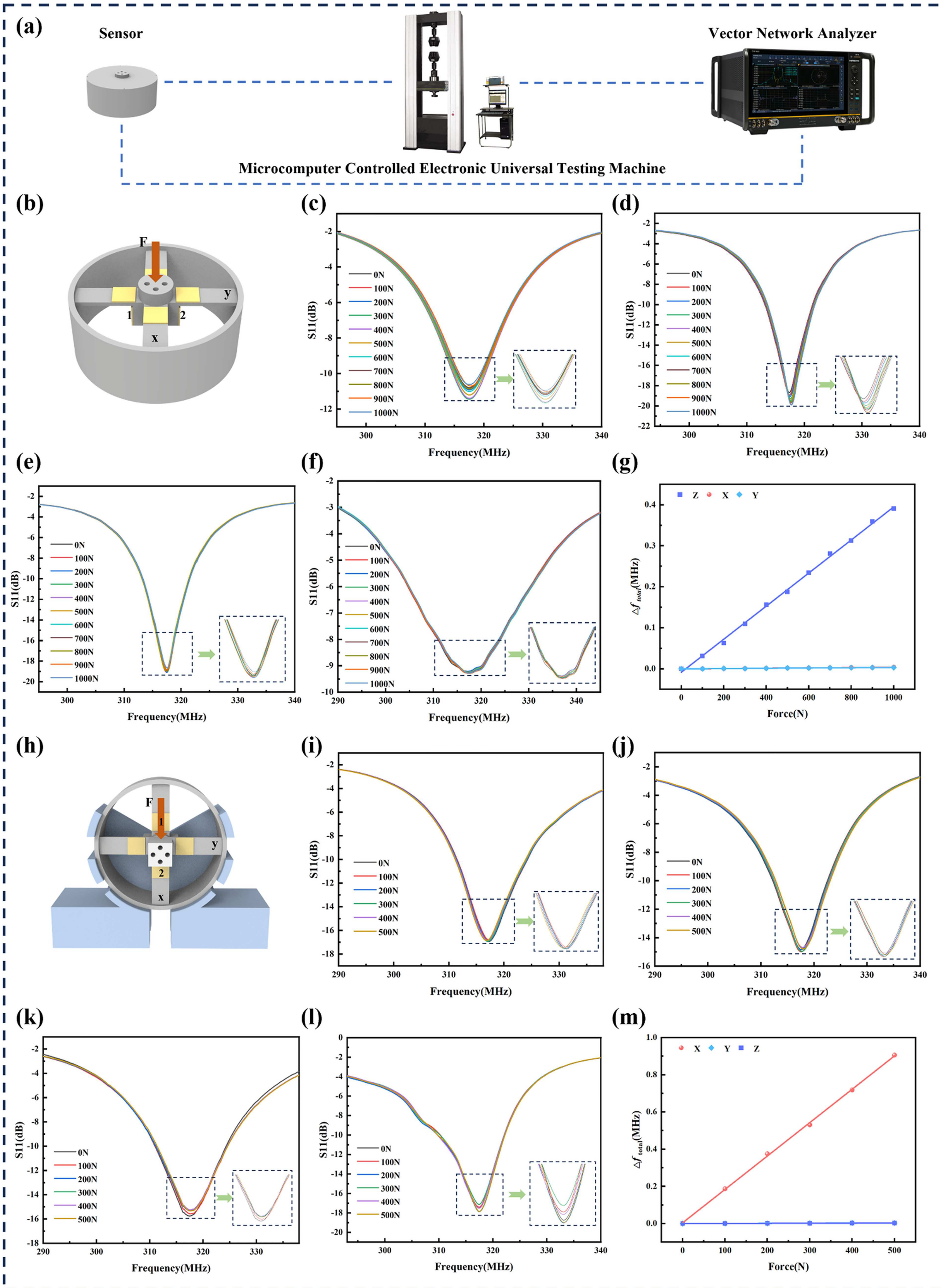

Figure 4 (Color online) Performance of the SAWMFS. (a) Test equipment; (b) sensor orientation for Z-axis loading; S_{11} curves at different forces (c) Z_1; (d) Z_2; (e) X_1; (f) Y_1; (g) output frequency change fitting curve; (h) sensor orientation for X-axis loading; S_{11} curves at different forces (i) X_1; (j) X_2; (k) Y_1; (l) Z_1; (m) output frequency change fitting curve.

can be approximated by the linear relation in (11). The slopes extracted from the three single-axis calibrations (corresponding to F_x, F_y, and F_z) are assembled to form the equivalent 3×3 sensitivity matrix. The diagonal terms represent the primary sensitivities of the three axes, whereas the off-diagonal terms quantify the residual coupling under single-axis loading.

$$\begin{cases}\Delta f_X = S_{Xx}F_x + b_X,\\ \Delta f_Y = S_{Yx}F_x + b_Y,\\ \Delta f_Z = S_{Zx}F_x + b_Z,\end{cases} \tag{11}$$

$$S = \begin{bmatrix} S_{Xx} & S_{Xy} & S_{Xz}\\ S_{Yx} & S_{Yy} & S_{Yz}\\ S_{Zx} & S_{Zy} & S_{Zz}\end{bmatrix}. \tag{12}$$

A normal load of 0–1000 N was applied along the Z-axis, and the frequency responses of the SAW devices were recorded for analysis. As shown in Figure 4(b), the normal force is transmitted through a loading column, deforming the internal structure and shifting the resonant frequencies of the bonded SAW resonators. The S_{11} responses of SAW-Z_1, SAW-Z_2, SAW-X_1, and SAW-Y_1 are presented in Figures 4(c)–(f). With increasing normal load, the frequency response of the Z-axis pair increases in an approximately linear manner. These observations indicate that the compressive load induces the dominant Δf in SAW-Z_1 and SAW-Z_2. The Δf_{total}-Force curve (Figure 4(g)) further supports a pronounced and linear Z-direction response. In contrast, differential processing of the X and Y channels suppresses their apparent frequency offsets to near zero. Under a single-axis load F_j, the ratio of the i-axis output to the j-axis output defines the crosstalk coefficient, as shown in (13). In the crosstalk evaluation, F_j is typically taken at two reference points: zero load and full scale. The calculated crosstalk values are $C_{XZ} = 0.92\%$ and $C_{YZ} = 0.77\%$. Averaging the resonant frequencies f_{Z1} and f_{Z2} (Figure S4(a)) yields a Z-axis sensitivity of 403.41 Hz·N^{-1}. This averaging suppresses antisymmetric components and reduces random fluctuations arising from slight bending asymmetry or eccentric loading.

The sensor was subsequently subjected to a shear load of 0–500 N applied along the X-axis (Figure 4(h)). The corresponding S_{11} curves for SAW-X_1, SAW-X_2, SAW-Y_1, and SAW-Z_1 are shown in Figures 4(i)–(l). As the shear force increases, the resonant frequency of SAW-X_1 increases monotonically, whereas SAW-X_2 decreases substantially. The variations of f_{X1} and f_{X2} are plotted in Figure S4(b), and their differential output is given in (14).

$$C_{ij} = \left|\frac{\Delta f_i}{\Delta f_j}\right| \times 100\%, \tag{13}$$

$$\begin{cases}\Delta f = f_{X2} - f_{X1} = f_0 k_\varepsilon(\varepsilon_{X2} - \varepsilon_{X1}),\\ \varepsilon_{X2} = -\varepsilon_{X1} \approx \varepsilon,\\ \Delta f \approx 2 f_0 k_\varepsilon \varepsilon.\end{cases} \tag{14}$$

Let f denote the differential frequency, f_0 the nominal center frequency of each resonator at zero load and the calibration temperature, k_ε the frequency-strain coefficient, and ε_{X1} and ε_{X2} the strains at locations X_1 and X_2, respectively. The absolute strain magnitude is represented by $|\varepsilon|$. Placing two SAW resonators symmetrically on opposite sides of the cross-beam and using differential readout transforms equal magnitude, opposite sign strains into a unidirectional frequency difference. This configuration increases sensitivity by approximately a factor of two while reducing temperature drift and crosstalk induced by non-target loads, improving accuracy under X-axis shear loading. The resulting X-axis sensitivity is 1794.64 Hz·N^{-1}, with crosstalk coefficients $C_{YX} = 0.75\%$ and $C_{ZX} = 0.62\%$, indicating a highly linear response in shear.

The loading configuration for Y-axis tests is illustrated in Figure S5(a): the triaxial sensor was placed on the platform, and a 0–500 N shear force was applied along the Y-axis, producing Δf in SAW-Y_1 and SAW-Y_2. The corresponding S_{11} curves for SAW-Y_1, SAW-Y_2, SAW-X_1, and SAW-Z_1 are shown in Figures S5(b)–(e). As the shear force increases, the resonant frequency of SAW-Y_1 increases monotonically, whereas SAW-Y_2 decreases; the X- and Z-axis resonators change only slightly because no direct loads acted along those directions. The frequency variations for SAW-Y_1 and SAW-Y_2 are plotted in Figure S4(c). Differential processing yields a Y-axis sensitivity of 1607.14 Hz·N^{-1} and crosstalk coefficients $C_{XY} = 0.77\%$ and $C_{ZY} = 0.62\%$. Across the 0–500 N range, the Δf_{total}-Force curves remain smooth and are consistent with linear behavior under transverse loading.

The main performance indicators are summarized in Table 2. The sensitivity and intercept matrix are given by (15) and (16). A linear mapping between Δf and triaxial forces is established by fitting each axis over the selected linear interval, as expressed in (17). The triaxial forces can then be computed directly from the calibrated linear coefficients. The Δf is dominated by the load component along the corresponding axis, with only minor contributions from the non-corresponding axes. The inter-axis crosstalk remains below 1%, suggesting suitability

Table 2 Key performance indicators.

Indicator	Direction	X	Y	Z
Single sensitivity (Hz·N^{-1})	1	−829.55	−840.91	387.18
	2	977.27	806.82	395.29
Comprehensive sensitivity (Hz·N^{-1})		1794.64	1607.14	403.41
Crosstalk (%)	X	–	0.77	0.92
	Y	0.75	–	0.77
	Z	0.62	0.62	–

for low-coupling multidimensional force measurements. These results provide a reliable experimental basis and quantitative reference for the design and optimization of multidimensional force sensors.

$$S=\begin{bmatrix}1794.64 & 6.24 & 3.91\\ 7.85 & 1607.14 & 3.46\\ 6.24 & 5.35 & 403.41\end{bmatrix}, \tag{15}$$

$$\begin{bmatrix}b_X & b_Y & b_Z\end{bmatrix}=\begin{bmatrix}4464.28 & -0.24 & -255.81\\ -89.42 & 14880.95 & -142.18\\ -0.23 & -297.52 & -8522.73\end{bmatrix}, \tag{16}$$

$$\begin{cases}\Delta f_x = 1794.64\,F_x + 4464.28,\\ \Delta f_y = 1607.14\,F_y + 14880.95,\\ \Delta f_z = 403.41\,F_z - 8522.73.\end{cases} \tag{17}$$

In device selection and system design, response time sets an upper bound on the achievable signal bandwidth and control rate and is defined here as the time required for the output to reach 90% of its final value after excitation. The dynamic responses of a PZT and a resistive strain gauge are measured at a loading frequency of 1.6 Hz (Figure 5(a)). Because the SAW device cannot be evaluated experimentally, its response time is estimated theoretically.

$$\tau=\frac{2L}{R}, \tag{18}$$

$$Q=\pi f_0\frac{2L}{R}=\frac{f_0}{\Delta f_{3\ \mathrm{dB}}}, \tag{19}$$

$$\tau=\frac{Q}{\pi f_0}, \tag{20}$$

$$t_{90\%}=-\tau\ln(1-0.9)=2.3\tau. \tag{21}$$

Eqs. (18) and (19) are combined to obtain (20), in which L is the motional inductance (kinetic-energy storage of the acoustoelectric branch), R is the motional resistance (total energy dissipation), τ is the energy-decay time constant, f_0 is the resonant frequency (317.4 MHz), $\Delta f_{3\,\mathrm{dB}}$ is the 3 dB bandwidth of the SAW resonator (minimum measured value 2.219 MHz), and Q is the quality factor (ratio of stored to dissipated energy). Substituting these parameters gives a 90% rise time $t_{90\%}=0.329$ μs.

Under identical loading conditions, the three sensing technologies exhibit markedly different dynamics: the PZT patch settles in 0.368 s, the strain gauge in 1.47 s, whereas the SAW device is estimated to reach $t_{90\%}=0.329$ μs, corresponding to a speed advantage of roughly six to seven orders of magnitude. Although the strain gauges and the PZT elements are inexpensive and straightforward to implement, their slow responses often require compensation algorithms. By contrast, the microsecond-scale response of the SAW sensor enables MHz-scale readout bandwidth in the electrical domain, enabling radio-frequency filtering, high-speed sensing, and real-time signal processing.

Table 3 compares the proposed resonant SAW three-axis force sensor with representative piezoresistive, strain-gauge, piezoelectric, silicon-based capacitive, fiber Bragg grating, and existing SAW force-sensing schemes. Because the compared schemes differ in sensing mechanisms and readout dimensionality, the sensitivity and crosstalk metrics in Table 3 are reproduced as reported in the original references for side-by-side comparison. Overall, relative to piezoresistive and piezoelectric schemes with millisecond-level responses, frequency-encoded SAW sensing offers the potential for substantially faster dynamics. The proposed device demonstrates sensitivities of 1794.64, 1607.14, and

Table 3 Comparison of performance metrics among representative force sensor designs.

Sensitive components/material	Load range	Sensitivity (X, Y, Z)	Response time	Crosstalk (%)				Ref.
					X	Y	Z	
Piezoresistive sensor	X/Y −1–1 N Z 0–2 N	0.02087, 0.02147, 0.02232 N^{-1}	30 ms	–				[3]
Strain gauges	X/Y 0–140 N Z 0–100 N	0.04, 0.041, 0.094 $\mathrm{mV{\cdot}N}^{-1}$	–	X	–	2.1	0.3	[4]
				Y	2.4	–	0.2	
				Z	1.6	0.9	–	
PZT	1–9 N	0.1702, 0.1946, 0.2524 $\mathrm{V{\cdot}N}^{-1}$	4 ms	–				[8]
Silicon-based capacitive	0–2.5 N	0.53, 0.52, 0.27 $\mathrm{pF{\cdot}N}^{-1}$	–	X	–	0.72	0.46	[11]
				Y	0.9	–	0.58	
				Z	0.29	2.21	–	
Fiber Bragg	−5.72–5.72 N	43.7, −43.7, −30.8 $\mu\varepsilon{\cdot}\mathrm{N}^{-1}$	–	–				[12]
SAW	0–100 kPa	632.733 $\mathrm{ppm{\cdot}MHz}^{-1}$	–	–				[23]
SAW	X/Y 0–500 N Z 0–1000 N	1794.64, 1607.14, 403.41 $\mathrm{Hz{\cdot}N}^{-1}$	0.329 μs	X	–	0.77	0.92	This work
				Y	0.75	–	0.77	
				Z	0.62	0.62	–	

403.41 $\mathrm{Hz{\cdot}N}^{-1}$ in the $X/Y/Z$ directions, respectively, with a response time of 0.329 μs. Meanwhile, the inter-axis crosstalk under uniaxial loading ranges from 0.62% to 0.92%. Overall, the results indicate that the composite beam structure, combined with differential/averaged decoupling readout, suppresses inter-axis coupling while retaining fast response, making the sensor well suited for three-axis force sensing in rigidly mounted, high-load contact scenarios such as robotic end effectors.

Δf are read out by reproducing the resonator's operating conditions in the measurement loop (Figure 5(b)). The resonator is placed in a feedback loop that oscillates at its resonant frequency f_{SAW}. This signal is mixed with a programmable reference ($f_{\mathrm{REF}} = 316.4$ MHz), and only the difference component Δf is retained. After low-pass filtering, the resulting beat note maps the Δf to a measurable voltage. During loading tests, this voltage signal alone provides a differential frequency output proportional to the applied force. Figure 5(c) shows the voltage waveform of SAW-X_2 under 0–500 N shear loading, and Figure 5(d) plots the peak-to-peak voltage V_{pp} against frequency and force, demonstrating strong linearity. The host-computer interface is displayed in Figure 5(e). The X-axis trace exhibits a stepped profile, whereas the Y- and Z-axis traces remain nearly constant. Equivalent results for SAW-Y and SAW-Z are provided in Figures S6–S8. The integrated "RF-frequency-digital" readout chain simplifies signal acquisition and ensures long term stability of the force-frequency mapping. It further provides a straightforward frequency-domain readout pathway for the SAWMFS.

2.4 Application of the SAWMFS

Multidimensional force sensors are widely used in robotics, particularly for force measurement and robotic-arm grasping tasks. The in-house robotic arm used in this study carries a 1.5 kg payload, provides a working radius of approximately 442 mm, and achieves a positioning repeatability of ±0.1 mm. Its motion ranges (maximum speed $108^{\circ}{\cdot}\mathrm{s}^{-1}$) are ±179° for joints 1, 4, and 5, and ±126° for joints 2 and 3, yielding a workspace suitable for the tests shown in Figure 6(a). For a practical evaluation, the sensor is embedded at the robotic arm end-effector (Figure 6(b)) without modifying the laboratory force-frequency calibration. Continuous Cartesian trajectories are programmed, exploiting the arm's positioning accuracy to impose diverse end-effector poses. As indicated in Figure 6(c), the Z-axis output increases linearly, whereas the X- and Y-axis outputs are smaller. Additional trials are performed at different velocities with brief dwells for steady readings; Figures 6(d)–(g) show that the measured force-frequency response increases linearly with the commanded load. Throughout the experiment, the sensor output follows the expected load in each segment, and no obvious hysteresis or distortion attributable to vibration or assembly stress is observed, supporting reliable performance after integration. The original directional decoupling strategy also remains effective, with no significant assembly-induced crosstalk.

These results indicate that the SAWMFS reproduces its laboratory calibrated force-frequency mapping on the robotic arm without recalibration, maintaining real-time traceability of force variations and stable multi-axis measurement. The sensor thus shows good engineering portability and provides reliable, continuous force information for robotic control, assembly monitoring, and safe human-robot interaction.

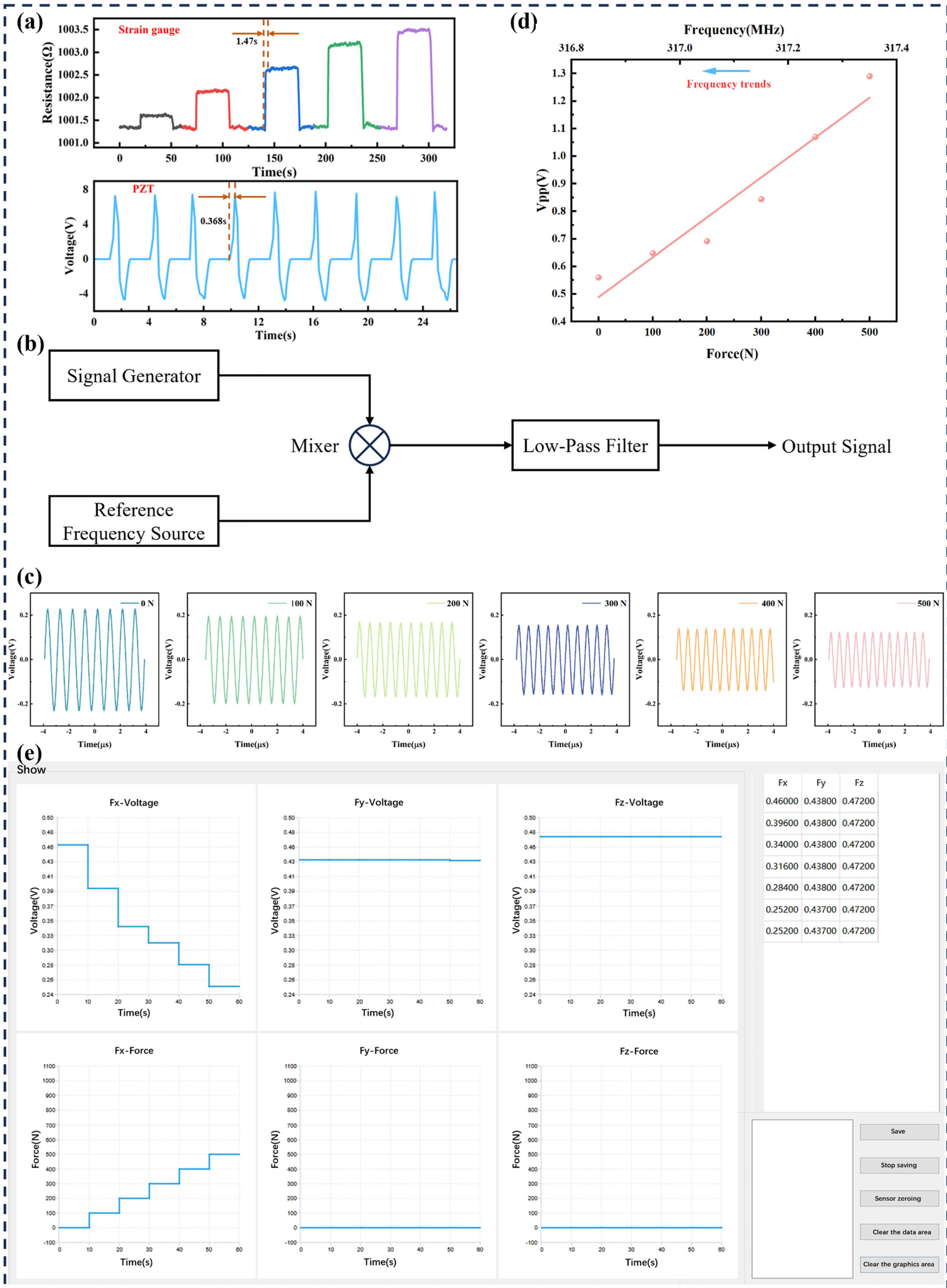

Figure 5 (Color online) Performance of the SAWMFS. (a) Response time comparison; (b) frequency-voltage conversion process; (c) SAW-X_2 voltage waveform; (d) V_{pp}-force/frequency fitting curve; (e) interface display F_x.

3 Conclusion

A high-load, high-precision multidimensional force sensor is presented by integrating resonant SAW devices on 128° YX $LiNbO_3$ into a cross-beam/vertical-beam composite structure. Two SAW resonators are symmetrically bonded on each horizontal beam pair to sense the X- and Y-axis, while another symmetric pair is mounted on the central vertical beam for Z-axis sensing. Differential readout for X/Y and averaged readout for Z convert opposite bending strains into co-directional Δf, suppressing common-mode disturbances and thermal drift to enable three-axis decoupling. A coupled electromechanical-acoustic model in COMSOL Multiphysics guides global optimization of beam thickness, inner-ring radius, and resonator placement, linking geometry design to signal processing. The sensor exhibits linear responses ($R^2 \geqslant 0.99$) over 0–500 N for X/Y and 0–1000 N for Z. The measured sensitivities

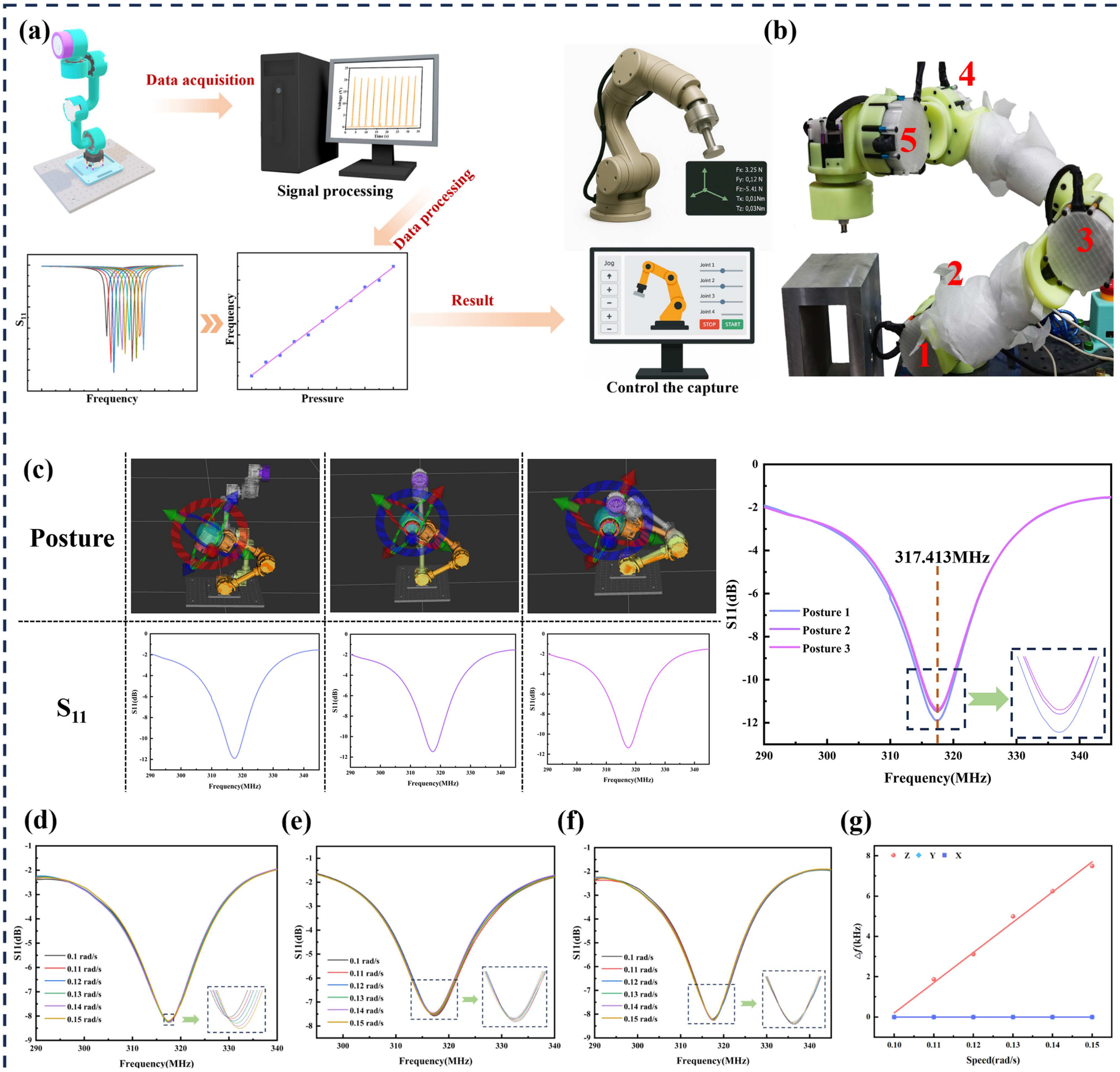

Figure 6 (Color online) Application of the SAWMFS. (a) Testing with a robotic arm; (b) physical robotic arm; (c) S_{11} responses at different postures; S_{11} responses at different speeds (d) Z_1; (e) X_1; (f) Y_1; (g) output fitting results.

are 1794.64, 1607.14, and 403.41 Hz·N^{-1} along X, Y, and Z axes, respectively, with cross-axis crosstalk below 1%. Only six resonators are required, eliminating the Wheatstone bridge; surface stress is encoded directly in frequency, improving robustness against noise and temperature drift relative to resistive strain-gauge readout. The SAW chips are only a few hundred micrometers thick, so added mass and stiffness minimally perturb beam dynamics. When integrated into a robotic-arm end effector for press-fit and collision tests, the sensor reproduces its laboratory force-frequency calibration without recalibration and supports high-rate triaxial force readout with microsecond-scale resonator dynamics. The proposed architecture is amenable to extension toward arrayed, multi-point tactile sensing. By distributing multiple sensor units across fingertips or grip surfaces, contact-force distribution and early slippage cues may be captured in real time. Future work will focus on array interconnection, miniaturized packaging, inter-unit decoupling, and system-level integration with compliant manipulators.

Acknowledgements This work was supported by National Natural Science Foundation of China (Grant Nos. 52305622, U2341210), Fundamental Research Program of Shanxi Province (Grant No. 202303021223008), and China Postdoctoral Science Foundation (Grant Nos. 2024M763033, 2025T180150).

Supporting information Figures S1–S8. The supporting information is available online at info.scichina.com and link.springer.com. The supporting materials are published as submitted, without typesetting or editing. The responsibility for scientific accuracy and content remains entirely with the authors.

References

1 Tao Y, Wan J, Song Y, et al. A safety posture field framework for mobile manipulators based on human-robot interaction trend and platform-arm coupling motion. Robot Comput-Integrated Manufact, 2025, 93: 102903
2 Wang G K, Liu Y H, Liu H P. One model, two skills: active vision and action learning model for robotic manipulation. Sci China Inf Sci, 2025, 68: 162202
3 Li D S, Li A M, Zhang Z B, et al. Highly sensitive MEMS three-dimensional force sensor for robot-assisted minimally invasive surgery. Sci China Tech Sci, 2025, 68: 1920301
4 Nguyen T H, Pham H T, Khoa Tran N D, et al. Design and characterization of a compliant six axis force/torque sensor with low cross-axis sensitivity. Measurement, 2025, 252: 117348
5 Zhang H, Yan Z, Zhang T, et al. Bioinspired high-linearity, wide-sensing-range flexible stretchable bioelectronics based on MWCNTs/GR/$Nd_2Fe_{14}B$/PDMS nanocomposites for human-computer interaction and biomechanics detection. ACS Sens, 2024, 9: 3947–3957
6 Wang X, Zhou H Y, Chen M H, et al. Wearable ultrasensitive and rapid human physiological monitoring based on microfiber Sagnac interferometer. Sci China Inf Sci, 2024, 67: 132403
7 Yu J B, Xian S, Mu J B, et al. Hybrid electromechanical properties of hetero-doped and homogeneously bonded dual-mode pressure sensor for indoor body area network node. Sci China Inf Sci, 2024, 67: 112401
8 Zhao F, Li T, Gu Y, et al. Flexible piezoelectric sensor enhanced by ordered piezoelectric composite material for three-dimensional force detection. ACS Appl Mater Interfaces, 2024, 16: 66543–66551
9 Xia L, Xiao W, Li L, et al. High-performance flexible capacitive pressure sensor based on a spiked nickel/polyimide composite nanofiber membrane. ACS Sens, 2025, 10: 1450–1460
10 Chu Z Y, Deng J, Su L, et al. A gecko-inspired adhesive robotic end effector for critical-contact manipulation. Sci China Inf Sci, 2022, 65: 182203
11 Tan R, Xia Y, Han X, et al. Miniaturized silicon-based capacitive six-axis force/torque sensor with large range, high sensitivity, and low crosstalk. Microsyst Nanoeng, 2024, 10: 180
12 Li Y, Tan T, Xie Y, et al. Self-decoupling six-dimensional force/ torque sensor based on fiber Bragg grating. Opt Lasers Eng, 2025, 188: 108896
13 Yu Q, Zhang Y N, Zhang J Q, et al. Smart fiber-optic masks: real-time respiratory monitoring and health analysis. Sci China Inf Sci, 2025, 68: 140408
14 Zhao J, Zhou H, Liu P, et al. Sensitivity enhancement for resonant multi-dimensional force sensor through integrated optimization of elastic structure and piezoelectric patch layout. Sens Actuat A-Phys, 2025, 392: 116691
15 Li X, Wang K, Wang Y, et al. A flexibility piezoelectric tactile sensor for three-dimensional force measurement. J Electrostatics, 2025, 136: 104101
16 Li Y, Xu X, Wang G, et al. Fault-tolerant measurement mechanism research on pre-tightened four-point supported piezoelectric six-dimensional force/torque sensor. Mech Syst Signal Process, 2020, 135: 106420
17 Yu G F, Liang R R, Zhao H M, et al. Geometry characteristics and wide temperature behavior of silicon-based GaN surface acoustic wave resonators with ultrahigh quality factor. Sci China Inf Sci, 2024, 67: 122402
18 Zhang Q, Wang Y, Li D, et al. Multifunctional and wearable patches based on flexible piezoelectric acoustics for integrated sensing, localization, and underwater communication. Adv Funct Mater, 2023, 33: 2209667
19 Chen Z, Zhou J, Tang H, et al. Ultrahigh-frequency surface acoustic wave sensors with giant mass-loading effects on electrodes. ACS Sens, 2020, 5: 1657–1664
20 Liu Q, Song Y, Wang F, et al. Ferroelectric domain reversal dynamics in $LiNbO_3$ optical superlattice investigated with a real-time monitoring system. Small, 2022, 18: e2202761
21 Duquennoy M, Fall D, Ben Jafela N, et al. A comparative study of divergent surface acoustic wave beams' generation on an Y128° lithium niobate using various types of interdigital transducers. Sensors, 2025, 25: 1067
22 Xu H, Cao Z, Dong S, et al. Flexible dual-mode surface acoustic wave strain sensor based on crystalline $LiNbO_3$ thin film. J Micromech Microeng, 2019, 29: 025003
23 Wang Z, Fu W, Qiao X, et al. SAW pressure sensor based on 128° Y-X-cut lithium niobate ferroelectric thin film with XGBoost temperature compensation. EPL, 2025, 150: 26003
24 Kubasov I V, Popov A V, Bykova A S, et al. Deformation anisotropy of Y + 128°-cut single crystalline bidomain wafers of lithium niobate. Russ Microelectron, 2017, 46: 557–563
25 Duan Z, Wang T, Ji W, et al. A2-mode lamb passive-wireless surface-acoustic-wave micro-pressure sensor based on cantilever beam structure. Sensors, 2025, 25: 1873
26 Kohler M C, Voiculescu I, Li F. Surface acoustic wave (SAW) force myography sensor for muscle force output identification. Sens Actuat A-Phys, 2024, 380: 115959
27 Li X, Tan Q, Qin L, et al. Novel surface acoustic wave temperature-strain sensor based on $LiNbO_3$ for structural health monitoring. Micromachines, 2022, 13: 912
28 Talbi A, Sarry F, Le Brizoual L, et al. Sezawa mode SAW pressure sensors based on ZnO/Si structure. IEEE Trans Ultrason Ferroelect Freq Contr, 2004, 51: 1421–1426
29 Xiao J, Chen G, Yuan Y, et al. Designing and optimizing method of SAW force sensor based on oneport resonator. In: Proceedings of the International Conference on Advanced Sensing and Smart Manufacturing (ASSM 2022), 2022. 215–224
30 Tseng K J, Li M H. Frequency and coupling factor scaling of shear horizontal SAW resonators in LNOI platform. In: Proceedings of the 2020 Joint Conference of the IEEE International Frequency Control Symposium and International Symposium on Applications of Ferroelectrics (IFCS-ISAF), 2020. 1–3
31 Chen X, Lv H, Zhang Y. A novel study on separation of particles driven in two steps based on standing surface acoustic waves. Chaos Solitons Fractals, 2022, 162: 112419
32 Geng W, Zhao C, Xue F, et al. Influence of structural parameters on performance of SAW resonators based on 128° YX $LiNbO_3$ single crystal. Nanomaterials, 2022, 12: 2109
33 Wu J, Zhang S, Ke X, et al. Rotated interdigital transducers with matched waveguide boundaries for high-performance surface acoustic wave devices. IEEE Trans Microwave Theor Techn, 2025, 73: 2490–2498
34 Hsu T H, Lee Z Q, Wu G L, et al. Gold as a promising electrode material for $LiNbO_3$-on-insulator (LNOI) SH-SAW resonators: an experimental study. IEEE Trans Ultrason Ferroelect Freq Contr, 2024, 71: 1324–1334
35 Song S, Wang Q, Zhou J, et al. Design of interdigitated transducers for acoustofluidic applications. Nanotechnol Precision Eng, 2022, 5: 035001
36 Shu L, Peng B, Li C, et al. The characterization of surface acoustic wave devices based on AlN-Metal structures. Sensors, 2016, 16: 526
37 Kuznetsova I E, Zaitsev B D, Borodina I A, et al. Investigation of acoustic waves of higher order propagating in plates of lithium niobate. Ultrasonics, 2004, 42: 179–182